Journal of Biomedical Optics 5(1), 23–30 (January 2000)

Super-resolution measurements with evanescent-wave fluorescence excitation using variable beam incidence

Dinah Loerke
Max-Planck Institute for Experimental Medicine,
D-37075 Göttingen, Germany

Beate Preitz
Max-Planck Institute for Experimental Medicine
D-37075 Göttingen, Germany

Walter Stühmer
Max-Planck Institute for Experimental Medicine
D-37075 Göttingen, Germany

Martin Oheim
Max-Planck Institute for Experimental Medicine
Göttingen, Germany
and Membrane Biology Group
University of Edinburgh
Scotland

Abstract. The evanescent wave (EW) elicited by total internal reflection of light selectively excites fluorophores in an optical slice above a reflecting dielectric interface. EW excitation eliminates out-of-focus fluorescence present in epiillumination microscopy, and—close to the coverslip—can offer a fivefold enhancement of axial optical sectioning compared to confocal and two-photon microscopy. The decay length of the evanescent field is a function of the refractive indices and light wavelength involved, and is modulated by the beam angle. EW microscopy was used to study the distribution and concentration of fluorophores at or near the interface in the presence of high concentrations in bulk solution. We modified an upright microscope to accommodate the condenser optics needed for EW excitation. Systematic variations of the angle of incidence were attained using an acousto-optical deflector, telecentric optics, and a hemicylindrical prism. The three-dimensional reconstruction of the fluorophore distribution from angle-resolved image stacks results in topographical information with an axial resolution of tens of nanometers. We applied this technique to study the axial position of dye-labeled subcellular storage organelles ('vesicles') of ≈300 nm diameter in the ''footprint'' region of living neuroendocrine cells grown on the interface. [S1083-3668(00)01101-1]

Keywords: total internal reflection fluorescence microscopy (TIRFM); evanescent wave; fluorescence; super-resolution; telecentric optics; exocytosis.

Paper JBO-90014 received Mar. 8, 1999; revised manuscript received Oct. 20, 1999; accepted for publication Nov. 1, 1999.

1 Introduction

The binding of molecules to surfaces, adsorption, catalytic reactions or biological processes like docking and fusion of synaptic vesicles, ligand-receptor binding, as well as the intracellular diffusion of second messengers are examples of molecular events that occur in the nanometer domain adjacent to the plasma membrane. When cells are grown on a glass coverslip, monitoring such events at single-molecule resolution has become possible with the introduction of evanescent-wave or total internal reflection fluorescence (TIRF) microscopy.[1–3]

The evanescent wave (EW) elicited by total internal reflection of a laser beam at a dielectric interface provides a means to selectively excite fluorescently tagged molecules very near to it. The intensity of the EW decays exponentially with distance from the interface with a typical decay length on the order of 100 nm. TIRF microscopy (TIRFM) therefore lends itself to the investigation of surface phenomena: The selective near-field excitation of fluorescence eliminates the out-of-focus light and bleaching present in conventional epifluorescence (wide-field) excitation and thus improves axial sectioning. Unlike confocal microscopes, TIRFM achieves its optical sectioning by confining the excitation light to a near-field volume so that wide-field detection can be used. Advantageously, it lacks the requirement for scanning. Due to the reduced light exposure and photodamage of the specimen, TIRFM allows long image series. At the same time, however, the strongest asset of TIRF imaging—the precise optical sectioning in axial direction—prevents a ''deep'' look into the specimen.

Owing to the exponential decay of the excitation intensity, axial position of fluorophores can be obtained with an unprecedented accuracy. This is even more true if information from images at different penetration depths is combined to reconstruct the concentration profile along the optical axis: the decay length of the near field is modulated by the beam angle of incident light θ_i. This modulation of the penetration depth of the EW by varying θ_i can be exploited to acquire images at different penetration depths. These θ_i stacks of images are then used to reconstruct the three-dimensional (3D) fluorophore distribution,[4–7] similar to the use of z stacks of images in wide-field 3D image reconstruction by iterative deconvolution techniques.

We have used a simple optical configuration to systematically vary the angle of incidence, based on an acousto-optical

The present address of Martin Oheim is Ecole Supérieure de Physique et Chimie Industrielles (ESPCI), 10 rue Vauquelin, F-75005 Paris, France. Electronic mail: martin.oheim@espci.fr
Address all correspondence to Dinah Loerke, Max-Planck Institute for Experimental Medicine, Hermann-Rein-Str. 3, D-37075 Göttingen, Germany. Electronic mail: dloerke@gwdg.de

1083-3668/2000/$15.00 © 2000 SPIE

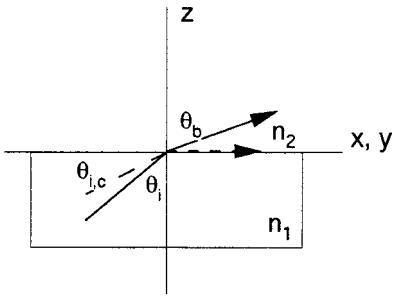

Fig. 1 Refraction of light at a dielectric interface between two media of differing refractive indices n_1 and n_1, where $n_1 > n_2$.

deflector, telecentric optics, and a hemicylindrical prism. Fast image acquisition and 3D reconstruction by fitting θ-resolved fluorescence data with the analytically determined Laplace transform allow topographical mapping even of dynamic specimens with an axial resolution of tens of nanometers. The only requirement is that the rate of image-stack acquisition is fast compared to the movement of the fluorophore.

We have used variable-angle total internal reflection fluorescence microscopy (VA-TIRFM) to study the secretion of hormones and peptides from neuroendocrine cells, a process that is believed to be comparable to the release of neurotransmitter into the synaptic cleft, the contact region between two brain cells. We could directly observe individual fluorescently labeled vesicles—membrane delimited storage organelles for neurotransmitter and hormones—in a living cell as they approach the cell membrane, bind to it, and—in response to stimuli—release their content into the extracellular space.[8,9]

2 Variable-Angle TIRFM

2.1 Total Internal Reflection

Light incident on a dielectric interface (from a higher to a lower refractive index medium) is refracted according to Snell's law (see Figure 1)

$$\sin\theta_i / \sin\theta_b = n_2 / n_1. \tag{1}$$

Light is totally reflected back into the higher refractive index medium if the angle of incidence exceeds the critical angle for total reflection, defined by Eq. (1) as

$$\theta_{i,c} = \sin^{-1}(n_2 / n_1). \tag{2}$$

For incidence angles above the critical angle, an evanescent field is created in the lower refractive index medium—a wave field, which decays exponentially with increasing distance from the interface and which penetrates only a fraction of the wavelength of light into the medium. The evanescent field intensity and the exponential decay constant (typically 30–300 nm) depend on the media refractive indices, the incidence angle, the illumination wavelength and the polarization angle. Considering the cosine of the deflection angle θ_b in Figure 1

$$\begin{aligned}\cos\theta_b &= \sqrt{1-\sin^2\theta_b} \\ &= \sqrt{1-(n_1^2/n_2^2)\sin^2\theta_i} = \sqrt{1-(\sin\theta_i/\sin\theta_{i,c})^2},\end{aligned} \tag{3}$$

it is clear that $\cos\theta_b$ becomes imaginary as soon as θ_i exceeds $\theta_{i,c}$. Then

$$\cos\theta_b = i\sqrt{(\sin\theta_i/\sin\theta_{i,c})^2-1}, \tag{4}$$

and the now complex phase of the refracted wave attenuates the wave in z,

$$\begin{aligned}\exp(i\mathbf{k}\cdot\mathbf{r}) &= \exp[i(k_x x + k_z z)] \\ &= \exp[i(kx\sin\theta_b + kz\cos\theta_b)] \\ &= \exp[ikx(n_1/n_2)\sin\theta_i] \\ &\quad\cdot\exp[-kz\sqrt{(\sin\theta_i/\sin\theta_{i,c})^2-1}],\end{aligned} \tag{5}$$

where $\mathbf{k}=(k_x,k_y,k_z)$, $\mathbf{r}$ is the position vector in the plane of incidence (x,z), $\mathbf{k}$ is the wave vector with $|\mathbf{k}|=k=2\pi/(n_2\lambda_0)$ denoting the wave number, λ_0 being the vacuum wavelength of incident light. The evanescent field generated by TIR illumination at the interface penetrates into the medium of lower refractive index; the field intensity decays exponentially with distance z from the interface,

$$I(z) = I(0)\cdot\exp(-z/d), \tag{6}$$

where the decay length

$$d = \frac{1}{2k\sqrt{(\sin\theta_i/\sin\theta_{i,c})^2-1}} = \frac{\lambda_0}{4\pi\sqrt{n_1^2\sin^2\theta_i - n_2^2}} \tag{7}$$

is a function of the refractive indices n_1 and n_2, respectively, the angle of incidence θ_i and the wavelength. The intensity of the evanescent wave field at the interface $I(0)$ is calculated by coherent superposition of the incident and reflected beam and solving Maxwell's equations for the appropriate boundary conditions.[10] It depends on the angle of incidence, the refractive indices, and the incident electric field amplitude A, so that

$$I_s(0) = |A_s|^2 4\cos^2\theta_i / (1-n_2^2/n_1^2), \tag{8}$$

for s-polarized light and

$$I_p(0) = |A_p|^2 \frac{4\cos^2\theta_i(2\sin^2\theta_i - n_2^2/n_1^2)}{(n_2/n_1)^4\cos^2\theta_i + \sin^2\theta_i - n_2^2/n_1^2}. \tag{9}$$

for p-polarized light (see Figure 2).[1]

2.2 Obtaining Depth Resolution: Variable-Angle TIRFM

The suppression of fluorescence excitation distant from the interface is not the only advantage when using evanescent-wave excitation; the dependence of the decay of the evanescent field intensity on the angle of incidence [Eq. (7)] can provide quantitative information about distances between fluorophores and the dielectric interface.[4,6,7,11,12] Whereas wide-field or confocal 3D imaging rely on stepping the focus up and down or scanning the beam with respect to the object space, respectively, in VA-TIRFM, systematic variations of the incidence angle allow depth-resolved measurements at a fixed focal position. The fluorescence signal obtained through

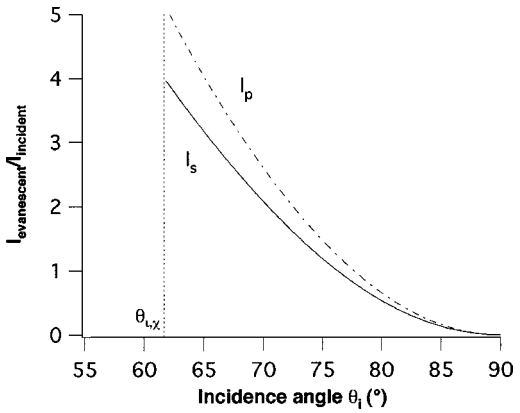

Fig. 2 Intensity of the evanescent wave at the interface ($z=0$) for linearly polarized light with an polarization angle parallel (I_p) and perpendicular (German: 'senkrecht', I_s) to the plane of incidence. Note the ''surface enhancement'' of the evanescent wave's intensity at the interface that can be several-fold that of the incident light. Field intensities are calculated according to Eqs. (8) and (9) (please note that in Ref. 1, the equations for the evanescent electric field components E_x and E_z—from which the above equations are derived—contain two minor typing errors). For the implemented setup geometry, the intensity at the interface is additionally modified by the angle-dependent deflection efficiency of the acousto-optic deflector used to scan the angle of incidence (see below).

the modulation of the penetration depth provides information about fluorophores located at different distances from the reflecting interface. If the frame rate is fast compared to the intrinsic dynamics of the specimen, the fluorophore z distribution can be recovered from image stacks acquired at different angles of incidence (θ stacks). VA-TIRFM permits measurements with an axial precision of tens of nanometers that has not been be achieved with previous 3D techniques.

2.2.1 *Quantifying VA-TIR-Excited Fluorescence*

Let $c_{x,y}(z)$ be the z distribution of fluorophores at each (x,y) position in the specimen plane. Then the measured fluorescence intensity $F_{x,y}(\theta)$ at a given pixel (x,y) of the image is given by

$$F_{x,y}(\theta)=I_{x,y}(0,\theta)\int_0^\infty C_{x,y}(z)Q(z)\exp[-z/d(\theta)]dz, \tag{10}$$

where $I_{x,y}(z=0,\theta)$ is the intensity of the evanescent field at the interface and $C_{x,y}(z)$ is a factor inclusive of $c_{x,y}(z)$, the quantum efficiency ϕ, and molar extinction ϵ. $Q(z)$ is the distance-dependent detection efficiency (see Figure 3).

For the 0.9 and 1.0 NA objectives, $Q(z)$ is roughly constant (Figure 3—see caption for a discussion of the limits of this approximation), so that Eq. (10) is, up to the preintegral factor, the Laplace transform of $C_{x,y}(z)$. Therefore, measuring $F_{x,y}(\theta)$ (i.e., taking fluorescence images for different angles of incidence) permits the subsequent recovery of $C_{x,y}(z)$ from $F_{x,y}(\theta)$ by inverse pixelwise Laplace transform, given that the angle-dependent function $I_{x,y}(0,\theta)$ [Eq. (8), Figure 2] can be eliminated from Eq. (10).[7]

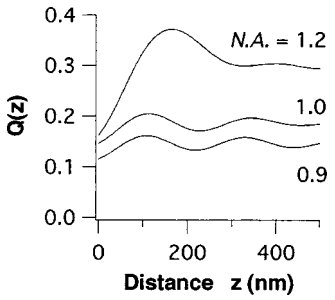

Fig. 3 Calculated distance-dependent collection efficiency for water immersion objectives with numerical apertures (NA) of 0.9, 1.0 and 1.2, respectively, located opposite the prism. Refractive indices were 1.52 for BK-7 glass and 1.34±0.1 for the cytoplasm. The theory for fluorescence emission at an interface (Ref. 11) was adapted to compute the distance-dependent collection efficiency (Ref. 7), $Q(z)$, introduced in Eq. (10). The calculated curves apply to the case of a fluorophore distribution with random dipole orientation excited by *s*-polarized light, and were obtained by numerical integration of the field equations for the particular objective lens' NA and the wavelengths used (488 nm/525 nm). Assuming $Q(z)$ to be constant introduces an error which, in the case of the 0.9 NA objective, is largest—about 15%—in a region between 50 and 100 nm distance from the interface, and then decays to below 5% by a distance of 160 nm (data not shown). In this study, we consider this error negligible for two reasons: Taking into account the size of granules and the fact that the cell membrane (even for very flat adherence) is located at several tens of nanometers distance from the coverslip, most of the fluorescent material is far enough away from the interface. Second, the remaining error is likely to be small or comparable to the error caused by local inhomogeneities in the evanescent wave by intracellular structures of varying refractive index. For increasing NA (see curves for NA 0.9, 1.0 and 1.2), the deviation from constancy is higher; it should be noted that the above calculation of $Q(z)$ is valid for fluorescence collection on the *lower-index side* of the interface only. Owing to the anisotropy of fluorescence emission, the distance dependence is even more pronounced when the objective lens is placed on the opposite side, i.e., underneath the reflecting interface, as in the prismless variant of TIRFM, in particular for numerical apertures exceeding the critical angle (Ref. 9).

2.2.2 *Eliminating Setup Parameters*

One strategy to get rid of $I_{x,y}(z=0,\theta)$ is to determine a function $F^{\mathrm{ref}}_{x,y}(\theta)$ from a known well-defined reference distribution of fluorophores. This is most easily accomplished using a homogeneous layer of dye solution, the thickness of which is large compared to the decay length d. Let $C^{\mathrm{ref}}_{x,y}(z)=C_{\mathrm{ref}}$ a constant that incorporates fluorophore concentration, quantum efficiency, and molar absorbency; then

$$\begin{aligned}F^{\mathrm{ref}}_{x,y}(\theta)&=I_{x,y}(0,\theta)\cdot C_{\mathrm{ref}}\cdot\int_0^\infty\exp[-z/d(\theta)]dz\\&\approx I_{x,y}(0,\theta)\cdot C_{\mathrm{ref}}\cdot d(\theta),\end{aligned} \tag{11}$$

where $Q(z)=\mathrm{const}:=1$ without loss of generality. Thus $I_{x,y}(0,\theta)$ can be eliminated by division of Eq. (10) by Eq. (11)

$$\begin{aligned}G_{x,y}(p)&:=F_{x,y}(\theta)d(\theta)/F^{\mathrm{ref}}_{x,y}(\theta)\\&=\frac{1}{C_{\mathrm{ref}}}\cdot\int_0^\infty C_{x,y}(z)\exp(-z\cdot p)dz.\end{aligned} \tag{12}$$

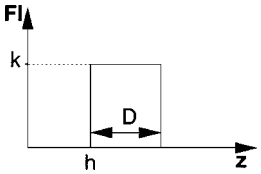

Fig. 4 Modeling axial fluorophore profiles with top-hat functions. Typical staining patterns that occur when labeling membranes, subcellular organelles or the cytosol can be modeled by varying the parameters of a rectangular function: $C(z)=\text{const}=c$ for $h \leqslant z \leqslant h+D$ and $C(z)=0$ elsewhere, with c the fluorophore concentration, h the distance to the reflecting interface, D the width of the distribution (e.g., the diameter of a secretory vesicle, or thickness of the membrane). For membrane-resident dyes, $D \rightarrow 0$, i.e., the top-hat function is approximated by a δ distribution at a distance h from the interface. Cytosolic dye, e.g., a Ca^{2+} indicator dye, is approximated by a layer of infinite thickness at distance h ($D \rightarrow \infty$), and extracellular staining is characterized by $h=0$.

$p := 1/d(\theta)$ defines the coordinate in the spatial-frequency domain. From a mathematical standpoint, numerically calculating the inverse Laplace transform of $G_{x,y}(p)$ allows us to determine the 3D fluorophore distribution $C_{x,y}(z)$. In the presence of measurement noise, this inversion becomes an ill-posed problem that is extremely noise sensitive.

Therefore, the introduction of a simple model of the axial concentration profile (see Figure 4) is a more practical way to analytically obtain the Laplace transform $G(p)$ and compare it with the measured function. For a sphere at distance h from the interface with $D \approx$ diameter d, the above model yields

$$G(p)=b+(k/p)\{\exp(-ph)-\exp[-p(h+d)]\}. \tag{13}$$

The result can then be fitted with the experimental data to yield parameters k (a dye concentration factor relative to C_{ref}), the distance h, the diameter d, and the integration and background constant b.

3 A Simple Optical Configuration to Control the Angle of Incidence

3.1 The 'Prism-Technique' Allows Beam Incidence at Variable Angles

A laser beam was guided at a supercritical angle onto the cell/substrate interface by directing it on the curved surface of a hemicylindrical BK-7 prism. The flat top of the prism was optically coupled to the fixed glass bottom of the recording chamber by a thin layer of index-matched immersion oil. The center of symmetry for the entire system was the midpoint of the flat top of the hemicylindrical prism, at which the laser beam was aimed at all times, regardless of the angle of incidence. The microscope, prism and laser optics (details below) were moved together as a unit, relative to a fixed stage, on which the recording chamber and the micro manipulators used to hold the patch clamp headstage and pipette, application pipette, and amperometric detection electrode were located. In the following, the light path of the VA-TIRF microscope is described from the source of excitation light to the detector (see Figure 5).

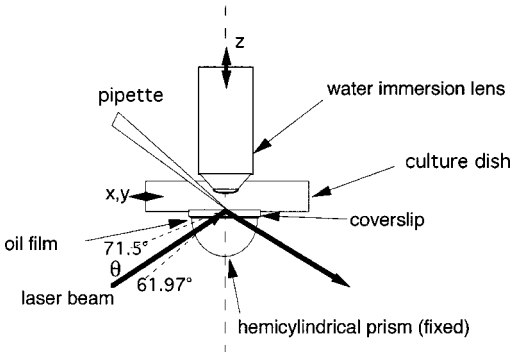

Fig. 5 Schematic of the prism approach of VA-TIRFM. The prism approach decouples the excitation from the collection optical path. The objective is located opposite the reflecting interface. Cells are placed in glass-bottomed holders coupled to the prism using low fluorescence immersion oil. Prism and objective are fixed and centered to the optical axis, whereas the chamber slides in the x,y plane on the oil film. The symmetry permits evanescent excitation at multiple angles of incidence while keeping the position of the illumination spot constant. In the case of cell studies, the glass pipette can be used for simultaneous electrophysiological measurements.

3.2 Light Path of the VA-TIRF Microscope

The main light source was a water-cooled 4 W argon-ion laser (L-3500, Lexel, Fremont, CA). The beam radius ($1/e^2$ intensity) at 488 nm TEM00 was 1.0 mm. Fluctuations in the laser output did not exceed $\pm 0.2\%$ after warm up. A set of neutral density filters (Omega, Brattleboro, VT) was used to attenuate the laser intensity to ~ 1 mW pre-fiber. To minimize photo damage to cells, a mechanical shutter (Uniblitz, Optilas, Puchheim, FRG) restricted illumination to periods of data acquisition. To shield the microscope from vibrations of the cooling water flow, the laser was separated from the microscope by an optical fiber. Laser light was coupled into the single-mode fiber via a piezo-driven fiber launcher (Polytec, Waldbronn, FRG). The $1/e^2$ beam radius at the fiber output was 900 μm, with a divergence angle of 0.028°. The fiber preserved the linear polarization of light so that the light is s polarized at the reflecting interface. Its transmission efficiency was ~ 0.65 at 488 nm. A custom-built VA-condenser (see below) coupled the excitation light into the microscope. For wide-field illumination a polychromatic light source (T.I.L.L. Photonics, Planegg, FRG) delivered 12 nm excitation bands to the epifluorescence port of the microscope. An additional D488/10× cleanup filter (Omega) with 5 nm bandwidth was used in the excitation light path when monochromatic epi-illumination at 488 nm was required.

3.3 Control of the Angle of Incidence

The direction of the excitation beam propagation was normal to the curved prism surface. For the mid angle this direction was collinear with the optical axis (x_1, y_1, z_1) of the custom-built VA condenser (Micro bench, Spindler & Hoyer, Göttingen, FRG). The focal point of the beam was at the center $(x_2, y_2)=(0,0)$ of the flat surface of the coverslip, irrespective of the beam angle θ_i. Angle μ defined the exit pupil of the lens, n_{air}, n_1 and n_2 were the refractive indices of air, prism and aqueous solution, respectively (see Figure 6).

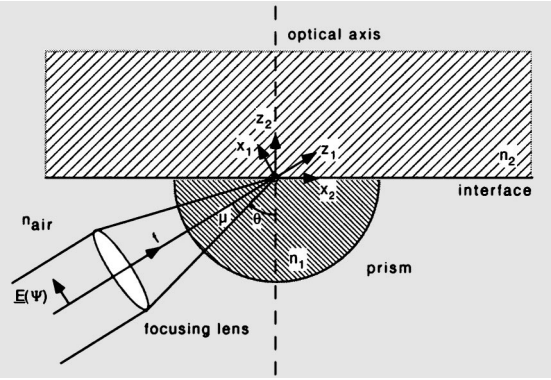

Fig. 6 Simplified geometry used to calculate the evanescent field intensity, making use of the approximation that the refractive indices of the prism, oil and coverslip are identical. The hemicylindrical prism ensures that the central ray is guided to the reflecting interface without refraction. The beam encounters the glass/water interface at the same location, irrespective of the angle of incidence. The ''spot'' of illumination in the interface plane (corresponding to a section through the focused Gaussian beam at the angle θ_i) is elliptical and varies in length with the incidence angle. The marginal rays of the focused beam are slightly refracted at the prism's outer surface (which acts as a cylindrical lens), resulting in a less precise focusing and slight enlargement of the spot size (see Ref. 8).

The incidence angle θ_i was measured from the normal to the prism's planar surface to the beam's central axis. The calculated critical angle was $61.97° \pm 1.2°$, assuming values of $n_2 = 1.33-1.36$ for the cytoplasm and $n_1 = 1.52(24)$ (at $\lambda_0 = 488$ nm) for BK-7 glass. Due to the uncertainty in n_2, $\theta_{i,c}$ was determined experimentally by increasing θ_i until TIR was observed. The goniometric table was adjusted with respect to this value with $5' = (1°/12°)$ accuracy. Small reproducible deflections of the incident beam were attained with an acousto-optic deflector (AOD) (Laser 2000, Wessling, FRG) and telecentric optics (Figure 7).

3.4 Acousto-Optic Deflection

An acoustic wave propagating in an optically transparent medium produces a modulation—a moving sinusoidal variation—of the index of refraction. For a light beam passing through it, this modulation acts as a diffraction grating. The acoustic wavelength in the medium Λ represents the spacing between compressions or rarefactions and therefore the grating constant δ. A light beam of wavelength λ_0 is diffracted into a number of orders at diffraction angles θ_d with

$$m\lambda_0 = d \sin \theta_d \quad (m \text{ integer}), \tag{14}$$

or, for a non-normal angle of incidence θ_i,

$$m\lambda_0 = d(\sin \theta_d - \sin \theta_i). \tag{15}$$

This condition becomes more selective for a three-dimensional grating, as in our case; at the Bragg angle, $\theta_d = -\theta_i$ a strong first-order ($m = 1$) maximum will occur so that

$$\lambda_0 = 2d \sin \theta_d. \tag{16}$$

The grating constant d of the AOD is defined by the acoustic wavelength Λ, so that

$$2 \sin \theta_d = \frac{\lambda_0}{\Lambda}. \tag{17}$$

Substituting $\Lambda = \nu/f$, where ν is the acoustic velocity and f the sound frequency,

$$2\theta_d = \frac{\lambda_0 f}{\nu}, \tag{18}$$

where the approximation $\sin \theta_d \approx \theta_d$ has been used. The beam deflection is proportional to the frequency of the sonic wave; also, the lower the acoustic velocity in the material, the larger the possible scan angle. TeO_2 with a sound velocity of one tenth that of BK-glass accomplishes this task. The scan angle was controlled directly from the image acquisition program; a $0 \ldots 10$ V signal was generated at the digital/analog (D/A) board (CIO-DAC02, Computer Boards, Mansfield, MA) of the imaging computer. The analog voltage tuned a variable-frequency driver (VFB-85-60-V-A-F.27-E, Brimrose, Baltimore, MA) in the range of 60–120 MHz. The AOD (Brimrose, TED10-85-60-.488-AR) was connected to the frequency driver via a 50 Ω impedance-matched cable. Frequency accuracy was 1% after warmup. A step change in tuning voltage resulted in a 50 μs delay from min to max deflection, making scanning speed irrelevant on the time scale of image acquisition. To achieve the first order diffraction efficiency of 75%, a careful alignment of the AOD with the incoming beam was required. A multiaxis miniature stage (Melles Griot, 07 TMC 521, Bensheim, FRG) facilitated this task. The central maximum was blocked at an aperture while the first order deflected beam was allowed to travel through a two-lens achromatic doublet to finally encounter the cylindrical lens (see Figure 7).

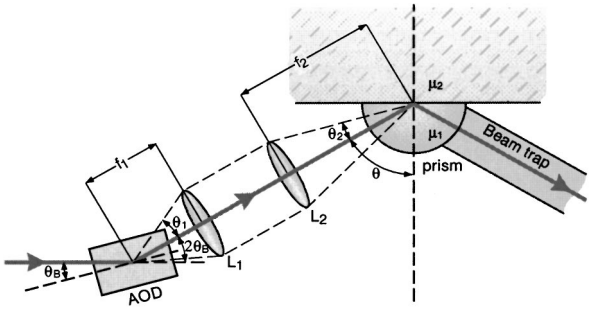

Fig. 7 Schematic of the telecentric optics used to keep the point of beam incidence fixed while varying the beam angle. A relay lens transforms the scan angle into a parallel beam displacement. The focusing lens (at an arbitrary distance of the first one) ensures that the beam converges to the midpoint of the hemicylindrical lens, irrespective of the incidence angle.

3.5 Telecentric Optics

In usual scanning devices, a beam emerges from a fixed point and is scanned along a cylindrical surface. In contrast, for VA-TIRF experiments, a geometry is favorable in which the location at which the laser beam is aimed remains fixed while the incidence angle is varied. This was accomplished by a system of two convex lenses. The exit pupil of the AOD is placed in the back focal plane of the first lens (L_1, achromate $f_1 = 15$ cm) so that the angular scan is converted to a parallel

displacement of the beam. This displacement is converted back to a change in beam incidence by placing the focus of the second achromate (L_2, $f_2 = 6$ cm) so that it coincides with the point at the dielectric interface at which TIR occurs. The two lenses (Spindler & Hoyer, Göttingen, Germany) form an achromatic doublet that minimizes aberrations. The ratio of focal lengths determines the final scan angle, 4.8°,

$$\theta_2 = \tan^{-1}[\theta_1(f_1 / f_2)]. \quad (19)$$

A hemicylindrical BK-7 ($n = 1.5224$) prism of 5.5 mm radius (Spindler & Hoyer) guided the incident beam without refraction to the same location on the stage of an upright microscope (Zeiss Axioskop, Jena, FRG). The prism was cut and polished to optical quality so that the midpoint of symmetry was at the upper surface of an index-matched coverslip of 0.17 mm thickness that was coupled to the prism's planar surface by a thin layer of immersion oil. To arrive at a reproducible thickness of the oil film, 3 μl of oil was applied to the prism's top with a micropipette. BK-7 coverslips ($n = 1.5224$) were purchased from Menzel (Braunschweig, FRG). Very low fluorescence oil (Leica, Bensheim, FRG, $n = 1.5180$) was preferred to precisely index-matched fluids (Cargille) with a higher autofluorescence. A 4 mm diam BK-7 glass rod (custom-made in the optics workshop, MPI Biophys. Chemistry, Göttingen, FRG) was optically coupled to the rounded site of the hemicylindrical prism with immersion oil, allowing for the reflected beam to leave the prism without significant reflection back to the flat top. The end of the rod was cut at an angle of 45° and mantled with black matte plasticine so that it acted as a beam trap.

3.6 Fluorescence Data Acquisition

Accurate focusing was achieved by a piezo-electric focus drive (Pifoc, P 721.20, Polytec). Objectives were either a Zeiss 100× 1.0 W NA or a 60× 0.9 W NA lens (Olympus, Hamburg, FRG). Fluorescence emission and scattered excitation light were separated by a dichroic and long-pass emission filter (all from Chroma Technology, Brattleboro, VT). Images were acquired with a 16-bit air-cooled charge-coupled device intensified camera (PentaMax, Princeton Instruments, Trenton, NJ). The GenIV image intensifier had a quantum efficiency of 0.37 in the range 520–580 nm. The frame-transfer chip (type EEV-37, 1024×512 pixel format) had 15 μm pixel size and $\geqslant$200 000 electrons full-well capacity. The 1:1.5 fiber coupler between the image intensifier and chip gives rise to an effective pixel size of 22.5 μm. Taking into account Rayleigh's definition of resolution and Nyquist's sampling theorem a diffraction-limited image on a single $(22.5\,\mu\text{m})^2$ pixel requires a total magnification of 2× pixel size× NA/(0.61λ), or an additional 1.51× and 1.12× magnification for the 1.0 NA 100× and 0.9 NA 60× lens. This was achieved by changing the microscope's tube lens using an Optovar (Zeiss). Maximum spatial sampling frequencies were 112.5 nm^{-1} (using the 100× objective and 2× tube lens) or 187.5 nm^{-1} (at 60×2×). Images were recorded in the frame-transfer mode at different frequencies, ranging between 10 Hz for standard acquisition (with on-line display and writing to the hard disk) and up to 200 Hz for ''stream'' acquisition. The chip was read out at 5 MHz. Digital image analysis was performed on a P55/200 MHz Pentium computer using the image acquisition and processing software METAMORPH 3.5 (Universal Imaging Corp., West Chester, PA). Modeling and mathematical analysis were done on a PPC8200/120 Macintosh computer using the macrolanguage IGOR (WaveMetrix Inc., Lake Oswego, OR).

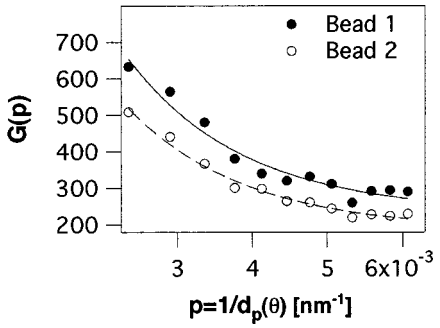

Fig. 8 $G(p)$ traces for two fluorescent microspheres located near the reflecting interface. $G(p)$ is the fluorescence intensity, normalized with the signal of a homogeneous and ''infinitely'' thick solution of reference dye (20 μM acridine orange). Spots and open circles represent measured values of $G(p)$, the solid line the calculated dependence of the (normalized) fluorescence on the angle-of-incidence.

4 Reconstruction of 3D Positional Information

Variable angle scans were performed on 18 nominally identical, stationary fluorescent latex beads on top of the glass/water interface. The specified diameter was 557± 11 nm (mean± SD). The function $G(p)$ was determined for each bead according to Eq. (12) from a stack of 34 images of 100 ms exposure time. The image stack of an angle scan of a homogeneous solution of acridine orange dye at the same position of the field-of-view was used as a reference signal, $FI^{\text{ref}}_{x,y}(\theta)$ (Figure 8). Lines represent the calculated $G(p)$ of a rectangular intensity fluorophore profile superimposed with the data (dots).

4.1 Reconstruction of Diameter, Distance and Relative Dye Concentration of Fluorescently Labeled Latex Beads

Figures 9(a)–9(d) compile the values of offset b, relative intensity k, distance h and diameter D for the 18 beads determined from a four-parameter free fit. Average values (mean ± SD) were $b = 223 \pm 57\ \text{nm}^{-1}$, $k = 5.0 \pm 3.0$ (AU), $h = 471 \pm 194$ nm and diameter $d = 550 \pm 27$ nm, respectively. Thus, bead diameters well below the conventional axial resolution limit were recovered accurately by four-parameter free fits. Distance and background parameters were normally distributed about the expected mean values.

4.2 Studying the Intracellular Dynamics and Location of Single Secretory Vesicles

Systematic variation of the incident angle offers control of the penetration depth d of the evanescent wave; in live chromaffin cells grown onto the interface, large penetration depths permit the evanescent excitation of regions somewhat deeper within the cell, while small penetration depths confine fluorescence excitation to the ''footprint'' of the cell.

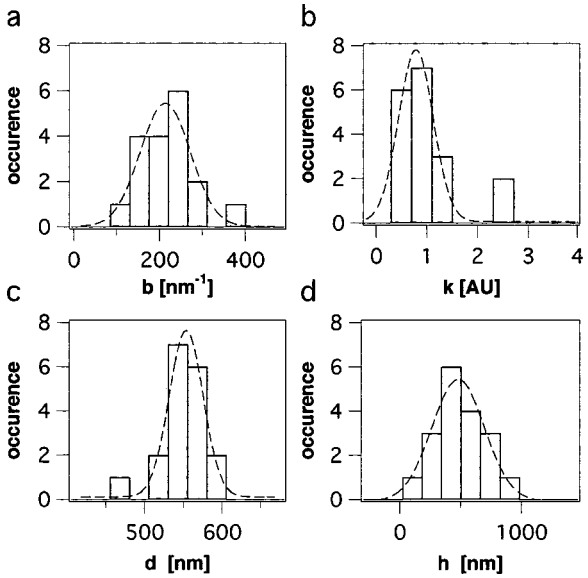

Fig. 9 To estimate the accuracy of the method, the parameters of well-defined fluorescent microspheres were determined. In four-parameter fits of the analytically derived $G(p)$ with the experimental data, parameters b, k, h, and d of Eq. (13) were determined simultaneously. The histograms show data pooled from 18 beads; for clarity, we superimposed Gaussian fits (dotted lines). (a) Histogram of the offset parameter b (which, by definition of $G(p)$, see Eq. (12), is measured in units of nm^{-1}.) (b) Parameter k incorporates the brightness, and—assuming homogeneously stained equally sized beads and a homogeneously lit field-of-view–allows a comparison of dye concentrations. (c) Histogram of measured diameters. The mean value, $D = 550 \pm 27$ nm reproduces the nominal diameter of 557 ± 11 nm with high accuracy, illustrating the possibility of subresolution measurements along the optical axis. (d) Recovered apparent distances from the reflecting interface.

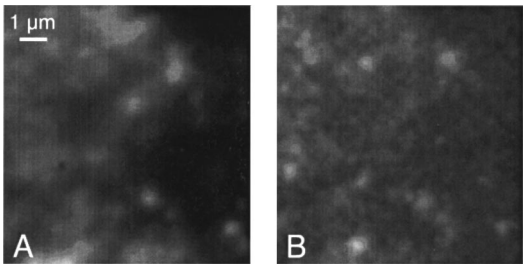

Fig. 10 Evanescent-wave excitation fluorescent images recorded at penetration depths of 124 and 84 nm. Like a bag of beans, chromaffin cells are densely packed with some 25 000 vesicles. Using conventional wide-field fluorescence microscopy, it is impossible to resolve single vesicles. In contrast, evanescent-wave excitation results in an efficient suppression of signal more than two decay lengths from the interface and allows us to highlight positions of individual vesicles near the reflecting interface. (Vesicles were stained by 3 min incubation of the cells in 5 μM acridine orange, a membrane-permeant dye that becomes trapped in acidic compartments).

VA-TIRFM allows the detailed reconstruction of the surface topography of cells grown to a coverslip. While in the image in Figure 10(a) fluorescent spots represent individual dye-labeled vesicles at an ≈ 100 nm distance from the interface, at a penetration depth of 84 nm [as in Figure 10(b)] fluorescence excitation is limited to the immediate vicinity of the reflecting interface so that only those vesicles in close apposition of the membrane are highlighted. Again, quantitative information on parameters of the 3D fluorophore distribution, e.g., the vesicle diameter, dye content and separation distance from the reflecting interface can be obtained from the analysis of the measured function $G(p)$.

5. Conclusion

TIRFM not only constitutes a sensitive assay for the detection of few molecules at an interface in the presence of high concentrations in adjacent volumes, but generally opens a window to the study of dynamics of subcellular structures in the near-membrane region. Due to the unprecedented axial optical sectioning, it allows us to determine the position of structures which had previously been hidden in a blur of fluorescence. While interference reflection microscopy can provide information on the cell's adhesion surface topography,[9,13,14] VA-TIRFM permits us to obtain nm 3D information in a thin cytoplasmic layer beneath the plasma membrane. Using fluorophores targeted to the membrane, cytoplasmic dyes, molecular markers,[9] or labeled organelles,[15] the accurate position and dynamics of specific structures can be highlighted.

TIRFM allows one to study spatial aspects of molecular interactions that have been inaccessible in living cells.[16] It can bridge the gap between existing cell biological assays for secretion on the one hand and biochemical *in vitro* studies of protein function on the other hand. Ever more specific fluorophores, novel detection schemes, and advances in digital image processing together will further extend our ability to understand dynamic processes and subcellular organization of living cells, potentially at single-molecule resolution.[17–19]

Acknowledgments

The authors would like to thank Dr. B. Ölveczky (UCSF) and Dr. J. A. Steyer (MPI, Heidelberg) for discussions on the distance-dependent collection efficiency, W. Lessner for expert technical support, F. Friedlein, M. Pilot, and B. Scheuffler for cell preparation, and L. Kolb and J. Ficner for help with some of the illustrations.

References

1. D. Axelrod, E. H. Hellen, and R. M. Fulbright, *Topics in Fluorescence Spectroscopy*, J. R. Lakovicz, Ed., p. 289, Plenum P, New York (1992).
2. N. J. Harrick, *Internal Reflection Spectroscopy*. 1st ed., Interscience, Wiley, New York (1967).
3. N. L. Thompson and B. C. Lagerholm, ''Total internal reflection fluorescence: applications in cellular biophysics,'' *Curr. Opin. Biotech.* **8**, 58–64 (1997).
4. J. S. Burmeister, G. A. Truskey, and W. M. Reichert, ''Quantitative analysis of variable-angle total internal reflection fluorescence microscopy (VA-TIRFM) of cell/substrate contacts,'' *J. Microsc.* **173**, 39–51 (1994).
5. W. M. Reichert, P. A. Suci, J. T. Ives, and J. D. Andrade, ''Evanescent detection of adsorbed protein concentration-distance profiles: Fit of simple models to variable-angle total internal reflection fluorescence data,'' *Appl. Spectrosc.* **41**(3), 503–508 (1987).
6. M. Oheim, D. Loerke, and W. Stühmer, ''Quantitative variable-angle total internal reflection fluorescence microscopy (VA-TIRFM) visualises dynamics of chromaffin granules with nanometer axial resolution,'' *Biophys. J.* **74**(2), A96 (1998).
7. B. P. Olveczky, N. Periasamy, and A. S. Verkman, ''Mapping fluorophore distributions in three dimensions by quantitative multiple

angle-total internal reflection fluorescence microscopy,'' *Biophys. J.* **73**, 2836–2847 (1997).
8. M. Oheim, D. Loerke, W. Stühmer, and R. H. Chow, ''The last few milliseconds in the life of a secretory granule. Docking, dynamics and fusion visualized by total internal reflection fluorescence microscopy (TIRFM),'' *Eur. Biophys. J.* **27**(2), 83–98 (1998).
9. J. A. Steyer, H. Horstmann, and W. Almers, ''Transport, docking and exocytosis of single secretory granules in live chromaffin cells,'' *Nature (London)* **388**, 474–478 (1997).
10. M. Born and E. Wolf, *Principles of Optics*, Pergamon P, Oxford (1980).
11. E. H. Hellen and D. Axelrod, ''Fluorescence emission at dielectric and metal-film interfaces,'' *J. Opt. Soc. Am. B* **4**(3), 337–350 (1987).
12. P. Suci and W. M. Reichert, ''Determination of fluorescence density profiles of Langmuir-Blodgett-deposited films by analysis of variable-angle fluorescence data curves,'' *Langmuir* **1988**(4), 1131–1141 (1988).
13. C. S. Izzard and L. R. Lochner, ''Cell-to-substrate contacts in living fibroblasts: an interference reflexion study with an evaluation of the technique,'' *J. Cell. Sci.* **21**(1), 129–59 (1976).
14. T. Gingell and I. Todd, ''Interference reflection microscopy. A quantitative theory for image interpretation and its application to cell-substratum separation measurement,'' *Biophys. J.* **26**, 507–526 (1979).
15. M. Oheim, D. Loerke, B. Preitz, and W. Stühmer, ''A simple optical configuration for depth-resolved imaging using variable-angle evanescent-wave microscopy,'' *Proc. SPIE* **3568**, 131–140 (1998).
16. R. D. Vale, T. Funatsu, D. W. Pierce, L. Romberg, Y. Harada, and T. Yanagida, ''Direct observation of single kinesin molecules moving along microtubules,'' *Nature (London)* **380**, 451–453 (1996).
17. T. Funatsu, Y. Harada, M. Tokunaga, K. Saito, and T. Yanagida, ''Imaging of single fluorescent molecules and individual ATP turnovers by single myosin molecules in aqueous solution,'' *Nature (London)* **374**, 555–559 (1995).
18. Y. Ishii, T. Yoshida, T. Funatsu, T. Wazawa, and T. Yanagida, ''Fluorescence resonance energy transfer between single fluorophores attached to a coiled-coil protein in aqueous solution,'' *Chem. Phys.* **247**(1), 163–173 (1999).
19. Y. Harada, T. Funatsu, K. Murakami, Y. Nonoyama, A. Ishihama, and T. Yanagida, ''Single-molecule imaging of RNA polymerase-DNA interactions in real time,'' *Biophys. J.* **76**(2), 709–715 (1999).